



Assembly and photochemical properties of mesoporous networks of spinel ferrite nanoparticles for environmental photocatalytic remediation

Euaggelia Skliri^a, Jianwei Miao^b, Jian Xie^c, Guangfeng Liu^c, Teddy Salim^c, Bin Liu^b, Qichun Zhang^c, Gerasimos S. Armatas^{a,*}

^a University of Crete, Department of Materials Science and Technology, Heraklion 71003, Greece

^b Nanyang Technological University, School of Chemical and Biomedical Engineering, 62 Nanyang Drive, Singapore 637459, Singapore

^c Nanyang Technological University, School of Materials Science and Engineering, Singapore 639798, Singapore



ARTICLE INFO

Keywords:

Cr(VI) reduction
Spinel ferrite nanoparticles
Mesoporous materials
Photocatalysis
UV-vis light

ABSTRACT

Spinel ferrite materials have an electronic band structure that is well suited for visible light-induced catalysis, however, their photocatalytic activity remains low due to the daunting charge-carrier separation process. In this article, we report that high-surface-area mesoscopic architectures composed of tightly connected ultrasmall spinel ferrite nanocrystals can efficiently suppress electron-hole recombination, manifesting an exceptional activity and magnetic recyclability in photocatalytic reduction of aqueous Cr(VI). Revealed by electron microscopy, N₂ physisorption, and X-ray scattering studies, the resulting materials, which were obtained through a block copolymer-assisted cross-linking aggregation of colloidal nanoparticles, show a 3D interconnected nanoporous structure with a large internal surface area (up to 159 m² g⁻¹) and exhibit small grain composition (ca. 6–8 nm in size). Through a systematic synthesis of various structural analogues to the spinel ferrite family and optical absorption and electrochemical impedance spectroscopy analyses, we demonstrate that the electronic band structure fits the electronic requirements for both Cr(VI) reduction and water oxidation under UV-vis light irradiation. Among spinel ferrites, ZnFe₂O₄ presents the highest activity, readily operating without additional sacrificial reagents in photocatalytic detoxification of aqueous Cr(VI), which together with transient gas analysis and fluorescence spectroscopy results suggest a competitive formation of oxygen and hydroxyl radicals at the catalyst surface. These findings provide an essential tool for the delineation of the electronic structure-catalytic property relationship in spinel ferrite nanostructures offering intriguing possibilities for designing new photocatalytic systems for efficient environmental pollution purification and energy conversion.

1. Introduction

Currently, contamination of natural water sources with hexavalent chromium, Cr(VI), arising from various industrial activities such as electroplating, metal finishing, and pigments, is an essential issue in environmental remediation field [1]. Cr(VI) is a mutagenic primer and pulmonary carcinogen for living organisms, with an LD₅₀ (lethal dose 50%) value of 50 mg kg⁻¹ [2], which readily invade the human food chains [3]. To this end, the World Health Organization (WHO) recommended a maximum allowable concentration of 50 µg L⁻¹ for Cr (VI) in drinking water [4]. Moreover, as a consequence of its high toxicity, hexavalent chromium has also been categorized as a Group I human carcinogen by the International Agency for Research on Cancer (IARC) [5]. Therefore, finding an effective way for remediation of Cr (VI)-contaminated solutions is undoubtedly of high priority in the field of environmental and health protection.

Towards this goal, semiconductor photocatalysis constitutes an intriguing technology to attain low-cost sustainable detoxification of Cr (VI) aqueous solutions using just the sunlight as an energy source. In this process, Cr(VI) oxyanions such as monovalent HCrO₄⁻ and divalent CrO₄²⁻ will be reduced to the less toxic Cr(III) cations by photoexcited electrons over a light-irradiated semiconductor catalyst. Simultaneously, the photogenerated holes on the surface of catalysts will be consumed in oxidation reactions. So far, a diverse set of semiconductor materials have been explored as Cr(VI) reduction photocatalysts, including ZnO [6], TiO₂ [7], CdS [8], WO₃ [9] and SnS₂ [10]. Although promising, studies on these systems, however, signifies the high recombination rate of photoexcited electron–hole pairs, low visible-light absorption in wide gap semiconductors and poor cyclic stability (e.g., metal sulfide catalysts are susceptible to photooxidation) as critical challenges to be addressed for practical applications. To increase the efficiency of photoreactions, recent efforts took advantage

* Corresponding author.

E-mail address: garmatas@materials.uoc.gr (G.S. Armatas).

from the modification of the semiconductor band structure by forming Schottky junctions with a narrow-bandgap semiconductor or a noble metal cocatalyst. In particular, these supplemental components can improve the charge-transfer separation processes within the semiconductor particles by acting as electron or hole collectors (through a band-edge potential gradient) [11,12]. Noble metal nanostructures could also provide access to redox pathways with low overpotential, thus further contributing to the high photocatalytic performance. Meanwhile, since most of the visible-light semiconductors have a valence band (VB) edge potential well above the water oxidation level, thermodynamic constraints may impede Cr(VI) photoreduction without the aid of suitable hole scavengers. Thus, several studies make use of sacrificial reagents, such as ethylenediaminetetraacetate (EDTA), ascorbic acid and ammonium compounds, to provoke Cr(VI) photocatalysis [13]. Since oxidation of these organic compounds is thermodynamically more favorable than water oxidation reaction, this process may overcome the competitive four-electron conversion of water to dioxygen and eventually enhance the kinetics of the Cr(VI) reduction [14]. Even though the hybridization of semiconductor structure or introduction of electron donor additives would exert efficient photocatalysis, these processes can impart an additional cost for the fabrication and operation of catalysts, which is a critical issue. Thus, it is highly desirable to develop a photocatalyst to achieve high Cr(VI) reduction efficiency at low cost, using the sunlight.

Spinel ferrite oxides (MeFe_2O_4 , where Me is a divalent metal ion such as Mn^{2+} , Co^{2+} , Fe^{2+} , Ni^{2+} , Zn^{2+} , etc.), due to their unique electronic and magnetic properties, are considered as a class of very promising materials for various technological applications. They have demonstrated great promise for applications in high-density magnetic storage devices, lithium-ion batteries, electrochemical capacitors and absorption of toxic metals (e.g., As(III), Pb(II), Hg(II)) because of their excellent redox behavior, high chemical stability (especially in acidic media), room temperature superparamagnetic or ferromagnetic activity, and large saturation magnetization (more than 50 emu g^{-1}) [15–21]. More recently, spinel ferrites, especially zinc ferrite (ZnFe_2O_4 , ZFO), have generated increasing interest as promising photocatalysts due to their narrow band gap ($E_g \sim 1.9\text{--}2.0 \text{ eV}$), favorable conduction band (CB) alignment for water splitting, good photochemical stability, low cost and easy magnetic separation [22–24]. As a consequence, ZFO-based materials have been exploited for photo-Fenton-like degradation of organic dyes [25–27] and photochemical hydrogen production [28,29]. Unfortunately, inherent problems of ZFO such as short hole diffusion length (ca. 10 nm), thus rapid recombination of photoexcited charges (electron-hole pairs), and low absorption coefficient still persist serious problems for its potential use in photocatalysis and energy conversion [30–32]. To address these limitations, the design and synthesis of spinel ferrite materials at the nanoscale featuring a large solid/liquid interface constitutes an efficient way. In principle, a semiconductor catalyst with small grain size composition can minimize the distance for photogenerated charges to transfer to the surface, and thereby to increase the separation efficiency of the free electron-hole pairs. On the other hand, since the optical absorption in most semiconductor materials (like metal ferrites) declines rapidly within about 15–20 nm, small-sized particles can absorb photons near the surface region and, thereby, facilitate charge separation at the catalyst/electrolyte interface. This means that a significant fraction of the photo-generated excitons would be available for redox reactions.

We have recently developed a method to assemble mesoporous networks of connected metal oxide nanoparticles (NPs). The synthetic procedure involves a polymer-templated self-assembly of colloidal NP building blocks followed by thermal annealing at elevated temperatures. This strategy is straightforward, cost-effective, and, more importantly, offers precise control over pore size, porosity and chemical composition of the assembled structures [33–36]. Of particular interest is that these porous materials exhibit the unique combination of accessible mesopores, small grain composition, and tunable visible light

response – all these characteristics are especially advantageous for constructing high-performance photocatalysts.

In this study, a series of mesoporous architectures of spinel ferrite NPs with an average diameter of 6–8 nm was synthesized using a block copolymer-assisted cross-linking aggregation of colloidal NPs and their impressive performance for photocatalytic detoxification of aqueous Cr (VI) solutions was demonstrated under UV and visible light illumination. In particular, we used different spinel ferrite nanobuilding blocks to construct open-pore network structures of connected NPs with large internal surface area and uniform mesopores. Systematic studies were conducted to elucidate the effect of morphology, electronic band structure and electrochemical properties of metal ferrite nanostructures on the Cr(VI) photoconversion efficiency. The photocatalytic reduction property of metal ferrites, especially Cr(VI) reduction, is rarely investigated. Herein, we show that mesoporous zinc ferrite (ZnFe_2O_4) assemblies, due to their unique three-dimensional (3D) porous structure, improved charge transfer along the NP-linked framework and proper matching of band-edge positions with respect to the Cr(VI) reduction and water oxidation potentials, exert outstanding performance in photocatalytic detoxification of Cr(VI). Furthermore, a possible mechanism for the overall photoreduction reaction of Cr(VI) is presented here by performing controlled experiments of fluorescence spectroscopy and oxygen evolution reaction coupled with mass spectrometry. These findings provide an insight into the activation of Cr(VI) detoxification catalysis through the use of suitable electron-donating reagents.

2. Experimental

2.1. Materials

Poly(ethylene glycol)-block-poly(propylene glycol)-block-poly(ethylene glycol) block copolymer (Pluronic P123, $M_n \sim 5800 \text{ g mol}^{-1}$), toluene (99.7%), absolute ethanol, sodium dodecylbenzenesulfonate (NaDBS, technical grade) and potassium dichromate ($\text{K}_2\text{Cr}_2\text{O}_7$, > 99.8%) were obtained from Aldrich Chemical Co. Sodium hydroxide (NaOH, 98%) and 3-aminopropanoic acid (3-APA, 99%) were purchased from Acros Organics. Iron (III) nitrate nonahydrate ($\text{Fe}(\text{NO}_3)_3 \cdot 9\text{H}_2\text{O}$, 98%), zinc (II) nitrate hexahydrate ($\text{Zn}(\text{NO}_3)_2 \cdot 6\text{H}_2\text{O}$, 98%), manganese (II) nitrate tetrahydrate ($\text{Mn}(\text{NO}_3)_2 \cdot 4\text{H}_2\text{O}$, 98%), nickel (II) nitrate hexahydrate ($\text{Ni}(\text{NO}_3)_2 \cdot 6\text{H}_2\text{O}$, 98%), cadmium (II) nitrate tetrahydrate ($\text{Cd}(\text{NO}_3)_2 \cdot 4\text{H}_2\text{O}$, 98%), cobalt (II) nitrate hexahydrate ($\text{Co}(\text{NO}_3)_2 \cdot 6\text{H}_2\text{O}$, 97.7%) and phenol (> 99.5%) were acquired from Sigma-Aldrich. All chemicals were used as received without further purification.

2.2. Synthesis of spinel ferrite NPs

Spinel ferrite (MeFO , Me = Zn, Mn, Ni, Cd and Co) NPs with an average diameter of 6–7 nm were prepared according to a modified literature procedure [37]. For a typical synthesis of ZFO NPs, $\text{Zn}(\text{NO}_3)_2 \cdot 6\text{H}_2\text{O}$ (5 mmol) and $\text{Fe}(\text{NO}_3)_3 \cdot 9\text{H}_2\text{O}$ (10 mmol) were dissolved in 25 mL of deionized (DI) water at room temperature, forming a clear solution. Next, 25 mL of 0.4 M NaDBS aqueous solution and 500 mL of toluene were added under vigorous stirring, and the resulting turbid solution was left overnight at room temperature, giving a clear solution. After that, 40 mL of 1 M NaOH aqueous solution was added dropwise to the above solution, which was stirred for another 2 h. Concentrated solution with suspended colloids was obtained by distilling out water and most of the toluene solvent, which then washed with water and ethanol several times to remove excess of surfactant. Subsequently, the product was isolated by centrifugation and then annealed under a nitrogen atmosphere at 350 °C for 12 h. The other spinel ferrite NPs, MnFe_2O_4 (MFO), NiFe_2O_4 (NFO), CdFe_2O_4 (CdFO) and CoFe_2O_4 (CoFO), were synthesized in a similar procedure, using the corresponding metal nitrate precursor.

2.3. Preparation of colloidal metal ferrite NPs

The surface of spinel ferrite NPs was modified with 3-APA according to a previously reported method [38]. Briefly, as-made MeFO NPs (230 mg) were added in 4 mL of DI water containing 3-APA (45 mg), and the pH of the solution was adjusted to 4.0 with 2 M HCl. The resulting mixture was then vigorously stirred at room temperature to assure that NPs will transfer to the liquid phase and form a stable suspension, typically within 24 h. The dispersion was initially assisted with sonication for about 20 min. The 3-APA-capped spinel ferrite NPs were isolated by centrifugation, rinsed several times with DI water, and finally dispersed in ethanol to form a stable colloidal solution of 120 mg mL⁻¹.

2.4. Synthesis of mesoporous spinel ferrite NP assemblies

The mesoporous spinel ferrite NP assemblies (MeFO MNAs) were synthesized as follows: 0.2 g of Pluronic P123 (EO₇₀PO₂₀EO₇₀) block copolymer was dissolved in 1 mL of anhydrous ethanol at room temperature. Then, 1 mL of colloidal MeFO NPs solution was slowly added to the surfactant solution under continuous stirring. The resulting mixture was kept at room temperature for 2 h and then stored in an oven at 40 °C for about 2–3 days under static condition. Mesoporous solids were prepared by heating the dry product in air for 4 h at 350 °C, using a 0.5 °C min⁻¹ heating rate. For comparison, untemplated ZFO material was also prepared by a similar procedure without the addition of polymer template. Bulk-like ZFO solid was also produced by thermal decomposition of Zn(NO₃)₂·6H₂O and Fe(NO₃)₃·9H₂O salts (in a molar ratio of 1:2, respectively) in air at 1100 °C for 2 h. The purity and crystal structure of as-prepared materials were confirmed with powder XRD.

2.5. Photocatalytic reactions

The photocatalytic Cr(VI) reduction was carried out in a Pyrex glass cell (100 mL capacity) containing 50 mL of Cr(VI) aqueous solution and different concentrations of catalyst (0.3–0.7 g L⁻¹). The Cr(VI) solution (50 mg L⁻¹) was prepared by dissolving K₂Cr₂O₇ in DI water, and the pH of the solution was adjusted to the desired values with dilute sulfuric acid. Before irradiation, the reaction solution was stirred in the dark for 30 min to ensure adsorption/desorption equilibrium and then exposed to UV-vis light, using a 300 W Xe lamp (Variac Cermax) equipped with cut-off filters (360 nm and 420 nm cut-off, respectively). All the experiments were carried out at 20 ± 2 °C using a water bath cooling system. During the reaction, the concentration of Cr(VI) in the solution was monitored via 1,5-diphenylcarbazide (DPC) colorimetric method, using a Perkin Elmer Lambda 25 UV-vis spectrometer. The normalized concentration (C_t/C₀) of Cr(VI) solution at different illumination times was calculated as proportional to the absorbance of DPC-Cr(VI) complex at 540 nm.

For the photocatalytic water oxidation reaction, 25 mg of ZFO MNAs catalyst and 50 mL of 50 mg L⁻¹ Cr(VI) aqueous solution (pH = 2) were placed into a 100-mL airtight quartz tube. The temperature of the suspension was maintained at 20 ± 2 °C by using an external water cooling system. The reaction solution was first purged with argon for 40 min under atmospheric pressure to remove any dissolved air and then irradiated with a 300 W Xe lamp ($\lambda > 360$ nm). The produced O₂ was analyzed by gas chromatography with a Shimadzu GC-2014 instrument equipped with a thermal conductivity detector, using Ar as a carrier gas.

2.6. Physical characterization

Thermogravimetric analysis was performed on a Perkin Elmer Diamond instrument in an air atmosphere (~200 mL min⁻¹ flow rate) with a heating rate of 5 °C min⁻¹. Small-angle X-ray scattering (SAXS) measurements were performed on a Xenocs Nano-inXider system using

Cu K α radiation ($\lambda = 1.54189$ Å). Scattering data were corrected for dark current and empty tube scattering. Powder X-ray diffraction (XRD) patterns were collected on a PANalytical X'Pert Pro MPD X-ray diffractometer (45 kV and 40 mA) using Cu K α ($\lambda = 1.5406$ Å) radiation (45 kV, 40 mA). Diffraction data were recorded in the 2 θ range of 20–80° with a 2 θ step size of 0.01° and a scanning speed of 0.1°/min in Bragg–Brentano geometry. Transmission electron microscopy (TEM) images were taken with a JEOL JEM-2100 electron microscope equipped with a LaB₆ filament and operated at 200 kV accelerating voltage. Samples were prepared by suspending fine powders in anhydrous ethanol and then drop casting on a copper grid covered with carbon film. Nitrogen adsorption and desorption isotherms were measured at –196 °C on a Quantachrome NOVA 3200e sorption analyzer. Before measurement, samples were degassed at 100 °C under vacuum (< 10⁻⁵ Torr) for 12 h. The specific surface areas were calculated using the Brunauer–Emmett–Teller (BET) method [39] on the adsorption data in the relative pressure range of 0.05–0.22. The total pore volumes were estimated from the adsorbed amount at the relative pressure (P/P₀) of 0.98 by applying the Gurvich rule, and the pore size distributions were obtained from the adsorption branch of the isotherms, using the non-local density functional theory (NLDFT) method [40]. UV-vis/near-IR diffuse reflectance spectra were recorded with a Perkin Elmer Lambda 950 optical spectrophotometer, using BaSO₄ powder as a 100% reflectance standard. The energy bandgap (E_g) of the samples were estimated from Tauc plots of (Fhv)² as a function of photon energy (hv), where F is the Kubelka–Munk function of the reflectance (R): F = (1 – R)²/(2R) [41]. Fluorescence spectra were obtained at room temperature on a Lumina Fluorescence spectrometer (Thermo scientific) equipped with a 150 W Xe lamp.

2.7. Electrochemical measurements

Mott–Schottky plots were collected with an electrochemical workstation (CHI 660E). A three-electrode set-up, with a platinum plate (1.0 × 2.0 cm²) and a silver–silver chloride (Ag/AgCl, 3 M KCl) as the counter and reference electrodes, respectively, was adopted to study the samples. The capacitance of the semiconductor/electrolyte interface was obtained at 1 kHz, with 10 mV AC voltage amplitude in 0.5 M Na₂SO₄ aqueous solution (pH = 7). Working electrode for impedance-potential measurements was fabricated as follows: ~10 mg of spinel ferrite catalyst was dispersed in 1 mL DI water and the mixture was subjected to sonication in a water bath until a uniform suspension was formed. After that, 40 μL of the suspension was loaded on the surface of fluorine-doped tin oxide (FTO, 10 Ω/sq) substrate, which was masked using 3 M scotch tape with an effective area of 1 cm². The sample was dried in a 60 °C oven for 30 min.

The donor density (N_d) of the semiconductors was calculated according to the Mott–Schottky equation:

$$N_d = \frac{2(d(1/C_{sc}^2)/dE)}{q_e \epsilon_s \epsilon_0} \quad (1)$$

where, ϵ_s , ϵ_0 are the relative dielectric constant of the material and the permittivity of vacuum, respectively, q_e is the electron charge, E is the applied potential, and C_{sc} is the space charge capacitance of the semiconductor.

3. Results and discussion

3.1. Structure and morphology

The synthesis of mesoporous assemblies of spinel ferrite NPs (hereafter denoted as MeFO MNAs, Me = Zn, Mn, Ni, Cd and Co) was accomplished by first modifying the surface of individual MeFO NPs with 3-aminopropanoic acid (3-APA) and then cross-linking the NP colloids in the presence of poly(ethylene oxide)-*b*-poly(propylene

oxide)-*b*-poly(ethylene oxide) (Pluronic P123, BASF) block copolymer. We confirmed the coordination of 3-APA to the NP surface with Fourier transform infrared (FT-IR) spectroscopy. Supporting Fig. S1 compares typical FT-IR spectra of 3-APA-capped ZFO NPs and pure 3-APA compound. The hybrid NPs show the carbonyl (C=O) stretching vibration bands of 3-APA at $\sim 1635\text{ cm}^{-1}$ and $\sim 1382\text{ cm}^{-1}$ region, which are slightly red-shifted by $\sim 5\text{ cm}^{-1}$ compared to that of pure 3-APA. Furthermore, there was no significant shift in the resonance of C–N ($\sim 853\text{ cm}^{-1}$) and –NH₂ ($\sim 1542\text{ cm}^{-1}$) bonds of 3-APA after surface modification. The IR analysis thus leads to a conclusion that the 3-APA ligands are being tethered to the NP surface through the carboxylate ($-\text{COO}^-$) groups, while the amine ($-\text{NH}_2$) functional groups are available to interact with the polar domains of the polymer template during synthesis. Mesoporous architectures of connected NPs with open-pore structure then obtained by annealing the polymer/NP composite samples in air at 350 °C to remove the polymer template and cross-link the NPs (through covalent bonding) into extended 3D networks (see Experimental section for details). Evidence that the template was entirely removed by calcination was obtained by thermogravimetric (TG) analysis. A typical TG curve of the mesoporous ZFO sample is shown in Supporting Fig. S2, where a weight loss of about 3.4% from 230 to 500 °C can be attributed to the hydroxylation of the particle surface.

The nanostructure of as-prepared spinel ferrite mesoporous materials was characterized by small-angle X-ray scattering (SAXS), X-ray diffraction (XRD) and transmission electron microscopy (TEM). A typical SAXS pattern of the mesoporous ZFO shows a weak broad scattering peak centered at q ($= 4\pi \times \sin \theta/\lambda$, where 2θ is the scattering angle) range of $\sim 0.47\text{ nm}^{-1}$ (Fig. 1a), which corresponds to an average repeat distance ($d = 2\pi/q$) of about 13.5 nm. The presence of this scattering peak indicates mesoscopic order, although with small coherent domain size, and corresponds to the center-to-center interparticle distance in the sample. Analysis of the scattering data with Guinier approximation [42] showed that the average diameter of constituent NPs is $\sim 8\text{ nm}$ (Fig. 1a, inset). XRD measurements revealed that the crystallinity of the precursor NPs, established through colloidal synthesis, well persists through assembly and annealing process. In Fig. 1b and Supporting Fig. S3, all the XRD diffraction peaks of mesoporous materials correlate well with the reference data for cubic metal ferrites. No peaks from impurity phase like ZnO or Fe₂O₃ had been detected in XRD patterns, indicating the phase purity of the samples. Using the Scherrer's equation and peak width of the (311) reflection, the average domain size of spinel ferrite crystallites in various mesoporous samples was calculated. In agreement with SAXS results, through this analysis, we obtained a grain size of about 6–8 nm (Table S1), which is very close to that of the respective precursor NPs (~ 6 –7 nm, see Fig. 1b and Supporting Fig. S4). These results reflect a minimal grain growth of crystallites during the high-temperature treatment.

TEM imaging has been used to investigate the morphology and microstructure of the assembled materials and typical results for mesoporous ZFO are shown in Fig. 1c and d. The TEM images depict a highly porous network composed of reasonably monodisperse NPs with an average diameter of 6–7 nm, which is in good accordance with the SAXS and XRD analyses. As shown in Fig. 1d, the NPs are interconnected forming a continuous structure, which allows a direct NP-to-NP contact for efficient charge transport. A typical high-resolution TEM (HRTEM) image displayed in inset of Fig. 1d further confirms the cubic spinel structure of the constituent NPs, showing distinct lattice fringes with $\sim 3.0\text{ \AA}$ spacing throughout the NPs that could be assigned to the (220) planes of cubic ZnFe₂O₄ structure. Meanwhile, selected-area electron diffraction (SAED) pattern taken from a part of the mesoporous network shows a series of broad concentric diffraction rings (Fig. 1e), signifying multiple orientations of small nanocrystals. All the electron diffraction rings can be readily assigned to cubic spinel phase of ZnFe₂O₄ with a lattice constant of $a = 8.429\text{ \AA}$ (space group: *Fd*-3m),

again supporting the single-crystalline nature of the ZFO MNAs. Further, energy dispersive X-ray spectroscopy (EDS) microanalysis of the inorganic network showed consistent results of the XRD and SAED; in Fig. 1f, EDS analysis of the ZFO MNAs indicated a stoichiometric ratio of Zn/Fe $\sim 1:2$ for constituent NPs, reaffirming a single-phase composition.

Nitrogen physisorption measurements revealed that our assembled structures have a high porosity with regular mesopores between the NPs. As shown in Fig. 2 and Supporting Fig. S5, all samples exhibit typical type IV adsorption-desorption isotherms with distinct H3-type hysteresis loop at a relative pressure (P/P_0) range of 0.45–1.0, which is characteristic of mesoporous solids with interconnected porosity. The Brunauer–Emmett–Teller (BET) specific surface areas and total pore volumes of mesoporous spinel ferrite materials were estimated to be 105 – $159\text{ m}^2\text{ g}^{-1}$ and 0.15 – $0.23\text{ cm}^3\text{ g}^{-1}$, respectively. These surface areas are very high if we account for their massive framework structure (mass density ~ 5 – 5.6 g cm^{-3}). The pore size distribution plots derived from adsorption data using the nonlocal density functional theory (NLDFT) model (based on slit-like pores) was found to be quite narrow with an average pore diameter of ~ 5 to 6 nm. The very similar pore size of the MeFO MNAs indicates proper replication of the assembled networks around the polymer template. Given an average SAXS repeat distance of 13.5 nm for ZnFO MNAs, from the difference between the interparticle distance and the pore size, we calculated a framework wall thickness of about 7.7 nm, which is highly consistent with the diameter of the constituent NPs ($\sim 8\text{ nm}$, as obtained from SAXS analysis). This implies that the walls of MeFO MNAs consist of a single layer of NPs. Table S1 summarizes the textural properties of the mesoporous samples. Note that the open mesopores and high surface area of the assembled structure of the MeFO MNAs offer a large catalyst/electrolyte interface area for fast mass-transfer kinetics and rapid electrochemical reactions, which are beneficial for the photocatalytic performance. With the purpose of elucidating the role of polymer template in the synthesis of spinel ferrite MNAs, untemplated ZFO sample has also synthesized by direct self-assembly of colloidal 3-APA-capped ZFO NPs and its textural properties were characterized by N₂ physisorption (details for synthesis are available in the Experimental section). This material exhibits a lower BET surface area ($81\text{ m}^2\text{ g}^{-1}$), pore volume ($0.14\text{ cm}^3\text{ g}^{-1}$) and average pore diameter (ca. 3.9 nm) than ZFO MNAs (Fig. 2), indicating that the proposed method is a typical template-driven synthesis process.

3.2. Photocatalytic study

3.2.1. Photocatalytic activity of MeFO MNAs

The photocatalytic activities of mesoporous spinel ferrite assemblies were assessed in the photoreduction of aqueous Cr(VI) solutions under UV–vis light irradiation. In Fig. 3, the evolutions of Cr(VI) photoreduction are plotted for the five different spinel ferrite catalysts. Compared to other mesoporous samples, ZFO MNAs is the most active catalyst toward Cr(VI) reduction giving a respective conversion level of $\sim 81\%$ in 3 h. As we shall discuss below, the high reactivity of ZFO relates to its highly porous structure and suitable electronic band structure for Cr(VI) reduction and water oxidation. Therefore, we focused on reactions with this catalyst during our further studies.

We proceeded to optimize the reaction conditions by changing the catalyst loading and pH of the solution. Supporting Fig. S6a shows the evolution of the photocatalytic reduction of Cr(VI) over time for different concentrations of ZFO MNAs catalyst. It can be seen that, with increasing catalyst concentration, the conversion of Cr(VI) is increased and reaches a maximum at 0.5 g L^{-1} . The increase photoactivity with the catalyst loading is due to the increased number of photons absorbed by the catalyst and the high density of surface active sites that are available for reaction [43]. However, the adverse effect on the photocatalytic activity upon further addition of catalyst (0.7 g L^{-1}) can be attributed to the light scattering from the particles surface.

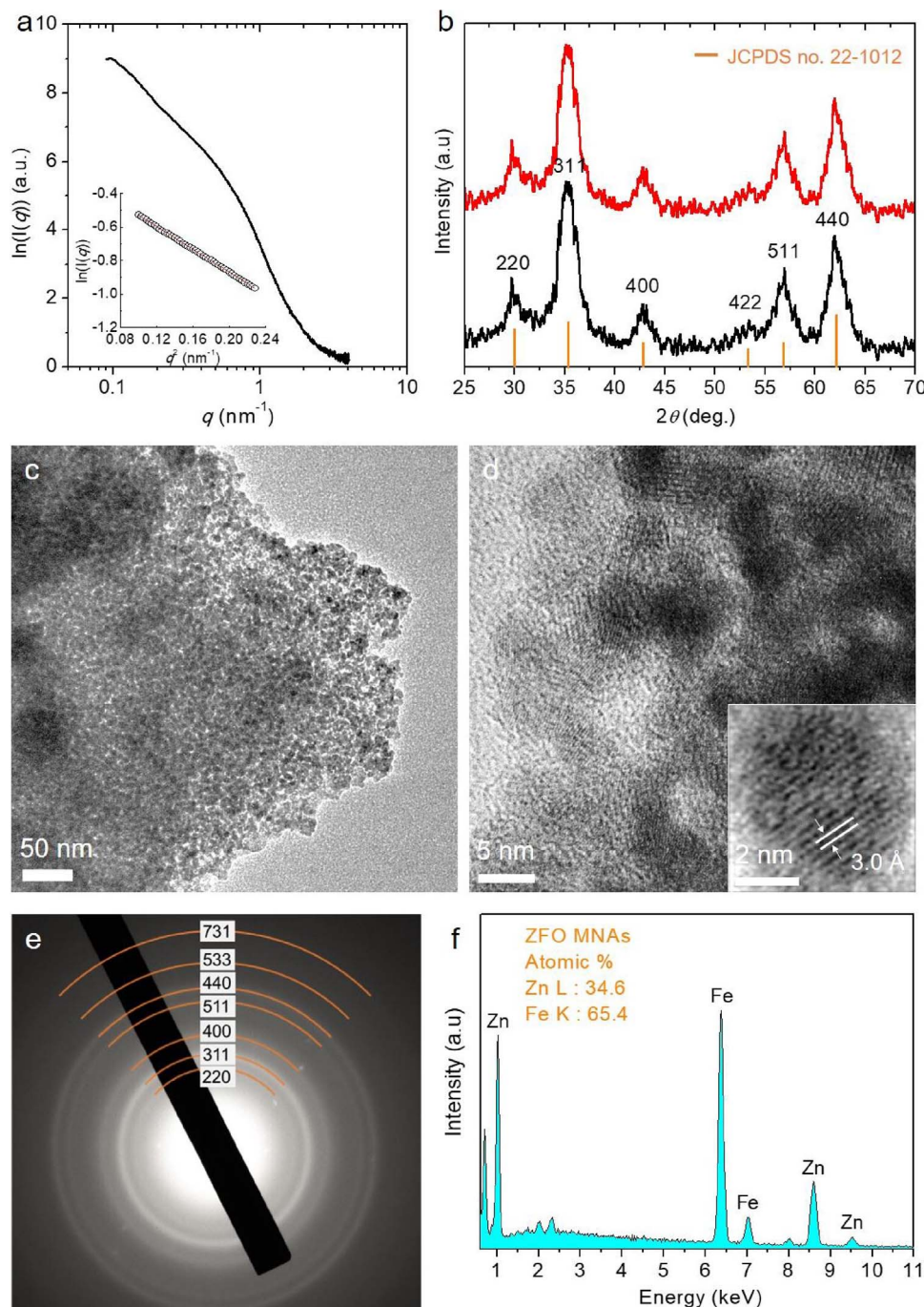


Fig. 1. (a) SAXS pattern (inset: Guinier plot, $\ln[I(q)] \propto q^2 R_g^2/3$, where R_g is the radius of gyration obtained from analysis of the low- q scattering data. The red line is fit to the data), (b) XRD pattern (black, lower line), (c) TEM image, (d) high-resolution TEM (inset: HRTEM of a single ZFO NP), (e) selected-area electron diffraction (SAED) and (f) typical EDS spectrum of mesoporous assemblies of ZFO NPs (ZFO MNAs). In panel b: the XRD pattern of precursor ZFO NPs (red, upper line) is also given. (For interpretation of the references to colour in this figure legend, the reader is referred to the web version of this article.)

Meanwhile, control experiments showed that no obvious reduction or adsorption of Cr(VI) occurs in the absence of light even after 3 h, demonstrating the photocatalytic nature of the reactions (see Fig. S6a).

Next, a series of catalytic experiments were performed to investigate the effect of pH on ZFO photocatalytic activity. As shown in Supporting Fig. S6b, the Cr(VI) reduction photocatalysis by ZFO MNAs remarkably increases as the solution pH decreases from 6 to 2. Notably, in a pH 2 solution, the ZFO catalyst achieves a Cr(VI) reduction level of ~81% in 3 h. We interpret the dependence of photoreduction rate on pH to the change in the Cr(VI) adsorption on the catalyst surface. The Cr(VI) species in low pH solution (precisely, less than 4) predominantly exist as HCrO_4^- anions, while in this environment the catalyst surface is positively charged; the point of zero charge (pH_{pzc}) of ZnFe_2O_4 is reported to be 4.6 [44]. This means that under acidic conditions ($\text{pH} < \text{pH}_{\text{pzc}}$) the surface of photocatalyst becomes positive ($\text{M}-\text{OH}_2^+$) due to

the excess of H^+ ions, which tends to adsorb more HCrO_4^- ions, thereby increasing the Cr(VI) photoreduction rate. As for the lower Cr (VI) reduction activity obtained at pH = 1, this could be attributed to the firm binding of the reactants (HCrO_4^- anions) or products (Cr(III) reduced species) of reaction by the catalyst surface.

3.2.2. Effect of morphology on the photocatalytic activity

The photocatalytic activity of ZFO MNAs remarkably exceeds that of the isolated ZFO NPs as depicted in Fig. 4a. The photocatalytic Cr(VI) reduction was investigated using similar amounts of catalysts (0.5 g L^{-1}) under identical conditions. Assuming that the reaction rate is proportional to the concentration of Cr(VI), the photocatalytic reaction can be expressed by the first-order kinetics of Langmuir-Hinshelwood model. Thus, analysis of the temporal evolution of Cr(VI) concentration using the pseudo-first-order reaction rate $[\ln(C_t/C_0) = -kt]$,

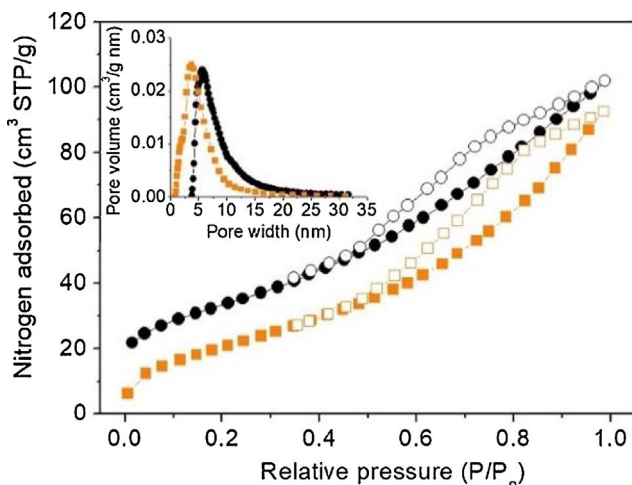


Fig. 2. Nitrogen adsorption (solid symbols) and desorption (open symbols) isotherms at $-196\text{ }^{\circ}\text{C}$ and the corresponding NLDFT pore-size distributions calculated from the adsorption branch of the isotherms (inset) for the ZFO MNAs (black symbols) and untempled ZFO material (orange symbols). The N_2 isotherms of the ZFO MNAs are offset by $5\text{ cm}^3\text{ g}^{-1}$ for clarity (STP: standard temperature and pressure). (For interpretation of the references to colour in this figure legend, the reader is referred to the web version of this article.)

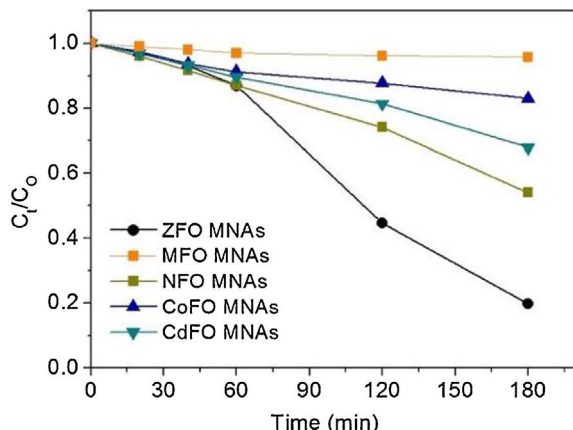


Fig. 3. Photocatalytic reduction of aqueous Cr(VI) over different spinel ferrite catalysts. The standard deviation of all measurements is about 3%. Reaction conditions: 500 mg L^{-1} catalyst, 50 mg L^{-1} Cr(VI) solution, pH = 2, UV-vis light ($\lambda > 360\text{ nm}$) irradiation, $20\text{ }^{\circ}\text{C}$.

where, C_t and C_0 is the concentration of Cr(VI) at initial time and time t , respectively, and k is the apparent reaction rate constant] reveals a rate constant k of $6.6 \times 10^{-4}\text{ min}^{-1}$ for ZFO NPs and $2.4 \times 10^{-3}\text{ min}^{-1}$ for mesoporous ZFO assemblies (see Fig. 4b). The lower photoactivity of isolated NPs might be ascribed to the agglomeration of NPs, which could form close-packed microstructures with a limited number of exposed active sites. Also, untempled ZFO sample, although has a sufficiently large surface area ($81\text{ m}^2\text{ g}^{-1}$), gave a lower conversion yield to Cr(III) ($\sim 46\%$ in 4 h, $k = 7.8 \times 10^{-4}\text{ min}^{-1}$). Presumably, a deterioration of Cr(VI) diffusion within the small interstitial voids (ca. 3.8 nm) may contribute to the slow reaction kinetics of untempled material. Consequently, all these results suggest that incorporation of small grain composition and high mesoporosity into ZFO catalyst has a beneficial effect in enhancing photocatalytic efficiency. In agreement to this, bulk-like ZFO particles (surface area $< 1\text{ m}^2\text{ g}^{-1}$), prepared by the direct calcination of $\text{Zn}(\text{NO}_3)_2$ and $\text{Fe}(\text{NO}_3)_3$ compounds at $1100\text{ }^{\circ}\text{C}$, show almost five times lesser photoreduction rate ($k = 5.1 \times 10^{-4}\text{ min}^{-1}$) than mesoporous ZFO assemblies.

Besides, the superior reactivity of the mesoporous ZFO assemblies as compared to isolated ZFO NPs could be attributed to the efficient

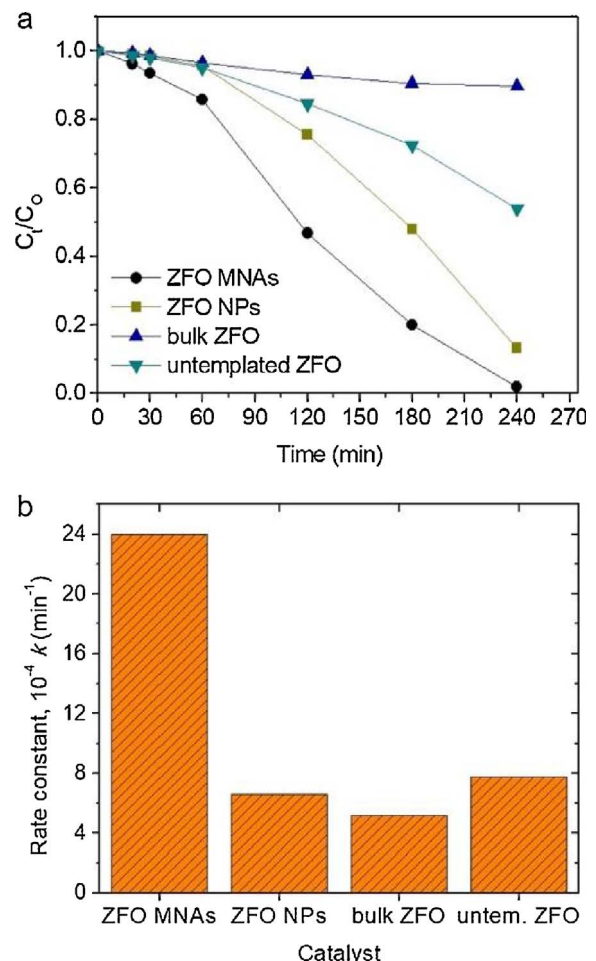


Fig. 4. (a) Photocatalytic reduction of aqueous Cr(VI) as a function of irradiation time (standard deviation = 3%) and (b) plot of kinetic rate constants (k) of mesoporous ZFO assemblies (ZFO MNAs), ZFO NPs, bulk-like ZFO solid and untempled ZFO material. Reaction conditions: 500 mg L^{-1} catalyst, 50 mg L^{-1} Cr (VI) solution, pH = 2, UV-vis light ($\lambda > 360\text{ nm}$) irradiation, $20\text{ }^{\circ}\text{C}$.

separation of photoinduced electron-hole pairs within the semiconductor network. This can be confirmed by comparing the photoluminescence (PL) spectra of colloidal ZFO NPs and ZFO MNAs. As seen from Supporting Fig. S7, the ZFO NPs exhibit an intense emission in the $390\text{--}500\text{ nm}$ range at room temperature when excited with photons of wavelength 325 nm . The PL peak at 380 nm corresponds to the interband electron-hole radiative transitions, while the weak shoulder peak at $\sim 480\text{ nm}$ arises from localized mid-gap states to the carrier relaxation processes due to intrinsic defects (particularly, interstitial Zn defects) [45]. Importantly, compared to isolated NPs, mesoporous ZFO assemblies show a dramatic decrease of the photoemission signal, indicating that recombination of photogenerated electrons and holes has been efficiently suppressed. These results suggest that the mesoporous framework of linked ZFO NPs has the potential to exhibits efficient charge transport between adjusted NPs, facilitating the electron-hole dissociation along the assembled structure. Notably, the photocatalytic activity of ZFO MNAs is superior or even comparable to that of other high-performance catalysts studied under similar conditions. A comparison of the photocatalytic Cr(VI) reduction activities of different catalysts is shown in Table S3.

3.2.3. Mechanism of photocatalytic Cr(VI) reduction

To better understand the hole transfer processes in spinel ferrite NPs, we also tested the photooxidation activity of ZFO MNAs under UV-vis light illumination. The photocatalytic water oxidation was

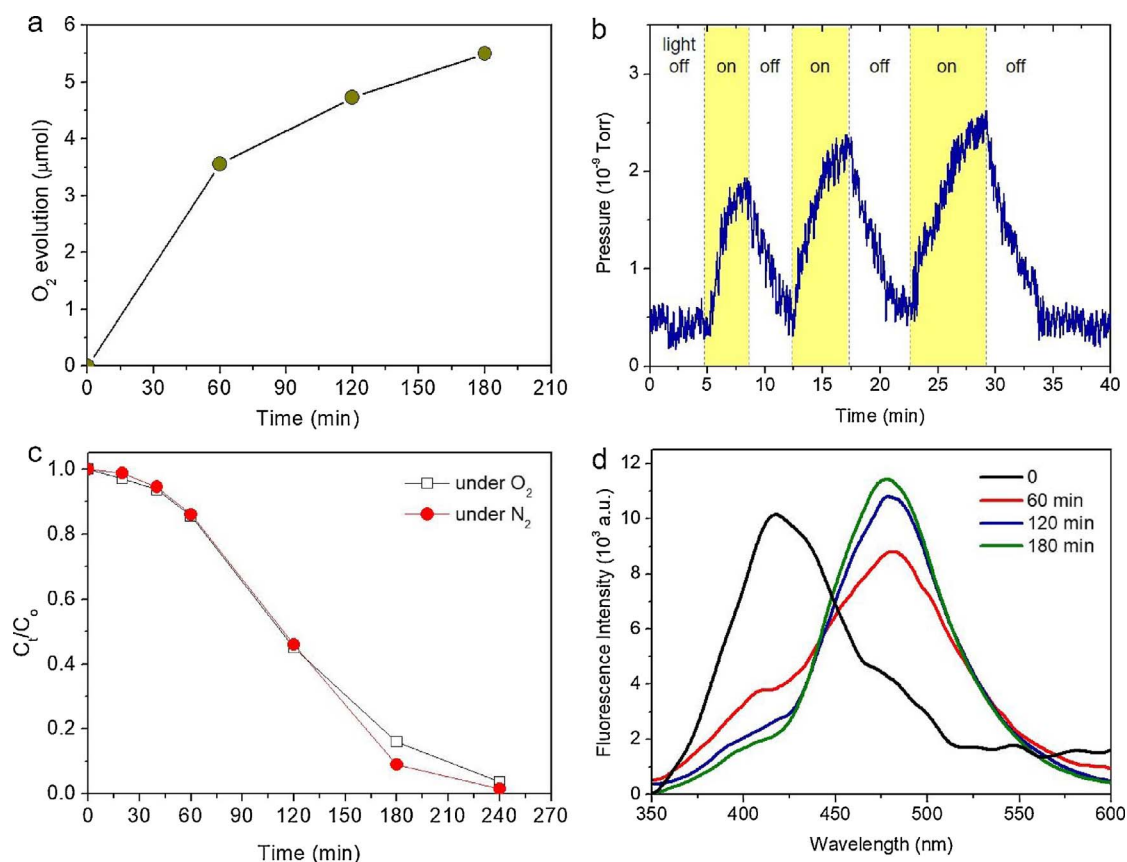
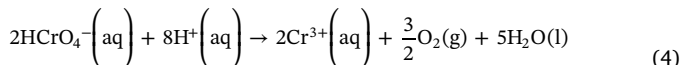
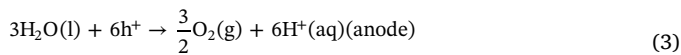
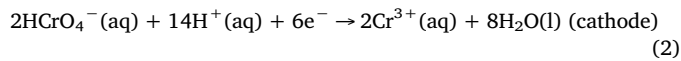


Fig. 5. (a) Photocatalytic oxygen evolution (standard deviation = 2.5%) and (b) O₂ evolution transient with light on/off for ZFO MNAs catalyst under $\lambda > 360$ nm light irradiation. (c) Influence of oxygen on the photocatalytic reduction of Cr(VI). The mean standard deviation for catalytic measurements is about 3%. (d) Fluorescence spectra of coumarin in water for ZFO MNAs catalyst. The emission peak at 395 nm and 455 nm corresponds to the coumarin and umbelliferone, respectively. Reaction conditions: 500 mg L⁻¹ catalyst, 10 mM coumarin (for control experiments shown in Fig. 5d), 50 mg L⁻¹ Cr (VI) solution, pH = 2, UV-vis light ($\lambda > 360$ nm) irradiation, 20 °C.

carried out in an air-tight quartz cell, and the evolved oxygen was analyzed by gas chromatography (Shimadzu GC-2014). As shown in Fig. 5a, ZFO MNAs catalyst is effective to oxidize water to dioxygen from an aqueous solution containing 50 mg L⁻¹ Cr(VI). This confirms that the photoreduction of Cr(VI) is largely associated with O₂ production; an average O₂ evolution rate of $\sim 2.6 \mu\text{mol h}^{-1}$ was obtained with 25 mg of ZFO MNAs catalyst after 3 h irradiation. To further verify that the detected O₂ was indeed generated by water oxidation reaction, we conducted the photocatalytic experiment, as described above, in a vacuum-tight cell and the generated oxygen was monitored in situ with a gas analyzer (Hiden HPR-20 QIC). Fig. 5b displays the transient photocatalytic O₂ evolution response of ZFO MNAs under light on and off conditions. It shows that oxygen quickly formed under UV-vis light irradiation, while no oxygen evolution is detected when the light was turned off. In conjunction with the results above, this study provides unequivocal evidence for the spontaneous water oxidation on the zinc ferrite surface, leading to the production of molecular oxygen. Thus, the overall reaction in acid conditions can be described in the followings Eqs. (2)–(4).



The photocatalytic Cr(VI) reduction activity of ZFO MNAs was also tested in an N₂-purged reaction cell (instead of under air atmosphere) to

gain information about the effect of oxygen on the Cr(VI) reduction kinetics. As seen from Fig. 5c, after 4 h of illumination, the conversion level of Cr(VI) reach $\sim 99\%$ (corresponding to an average Cr(VI) reduction rate of $3.9 \mu\text{mol h}^{-1}$), which is very similar to that obtained from the air-equilibrated system (ca. 98%, $4.0 \mu\text{mol h}^{-1}$ Cr(VI) reduction rate). These results clearly show that presence of oxygen has no influence on the reduction of Cr(VI), indicating that HCrO₄⁻ species preferentially accept electrons during the catalytic process, as anticipated from the higher (more positive) redox potential of HCrO₄⁻/Cr³⁺ (0.94 V vs. NHE, pH = 7) compared to O₂/O₂^{·-} (−0.33 V vs. NHE, pH = 7) [46].

Also, aside from the oxygen evolution reaction, photooxidation of surface hydroxyl groups may also proceed by a direct hole-transfer mechanism. In fact, in photocatalytic Cr(VI) reduction process, the photogenerated holes migrate to the surface of the catalyst, where they may react with hydroxyl (−OH) groups or adsorbed water molecules to form hydroxyl radicals (·OH). Recently, we have demonstrated that this is a viable possibility for CoO catalyst in the photocatalytic reduction of Cr(VI) [47]. To examine whether ·OH radicals are produced during the photocatalytic process, fluorescence spectroscopy was conducted using coumarin as a fluorophore. Coumarin is an excellent probe for monitoring the formation of hydroxyl radicals in a solution; it reacts with ·OH to produce umbelliferone which emits a characteristic fluorescence signal at 455 nm under 332 nm excitation. Fig. 5d displays the time-dependent emission spectra of the reaction solution, showing the progressive decrease in the emission of coumarin and the appearance of the emission band of umbelliferone. These results agree against the formation of ·OH under the photocatalytic Cr(VI) reduction conditions, which can be ascribed to the favorable oxidation of surface hydroxyl groups (E° (·OH/OH[−]) = 1.58 V) [48] and absorbed water

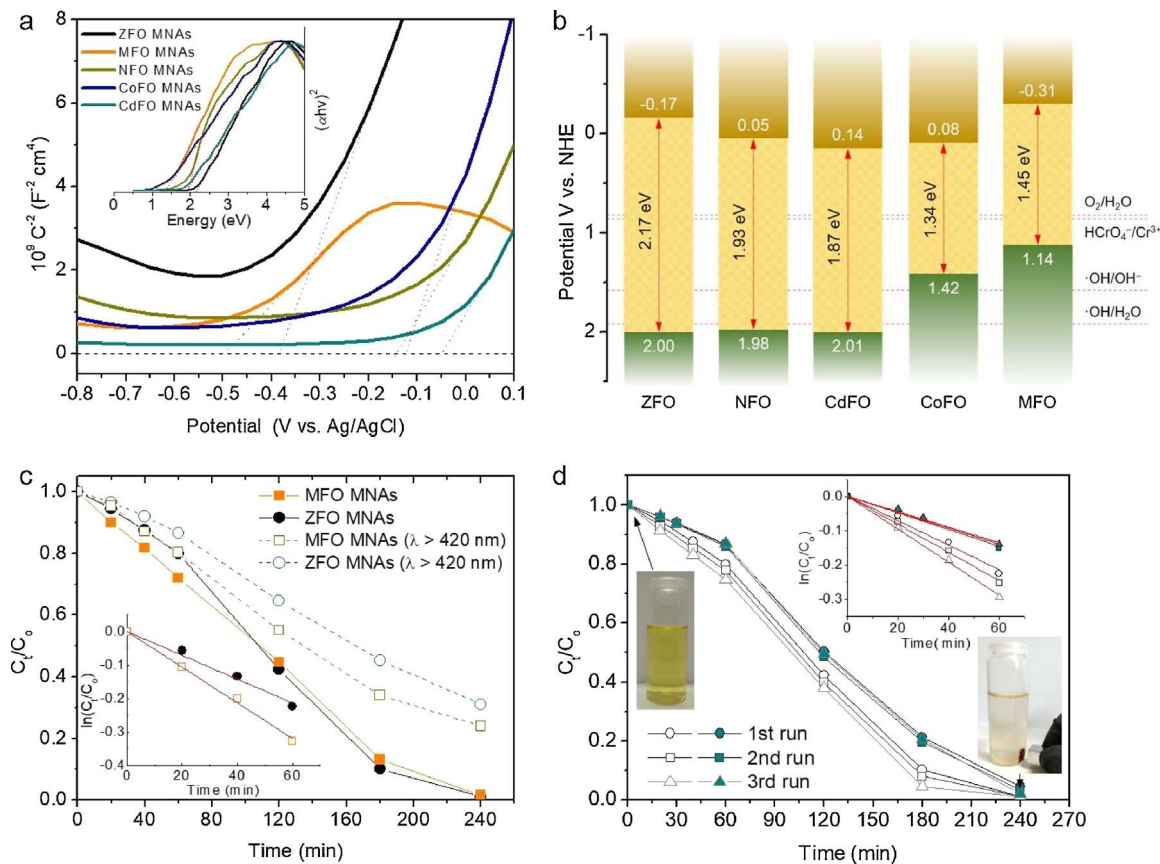


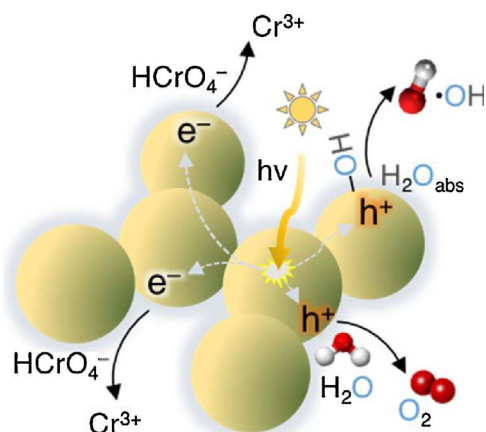
Fig. 6. (a) Mott-Schottky plots (Inset: the $(Fhv)^2$ versus $h\nu$ plots derived from optical adsorption spectra) and (b) energy band diagrams of mesoporous spinel ferrite MNAs catalysts. The red dashed lines are the tangents of the curves, showing the flat-band potential and energy bandgap of the semiconductors respectively. (c) Photocatalytic reduction of aqueous Cr(VI) with ZFO and MFO MNAs catalysts in the presence of phenol under UV-vis ($\lambda > 360$ nm) and visible ($\lambda > 420$ nm) light irradiation. (d) Recycling study of the ZFO MNAs catalyst in the absence (closed symbols) and presence (open symbols) of phenol (Inset photographs: initial solution of Cr(VI) and separation of the ZFO MNAs catalyst using an external magnet after reaction). The insets of panels c) and d) show the corresponding kinetic plots of the pseudo-first-order reaction rates. The red lines are fit to the data. The mean standard deviation for catalytic measurements is about 3%. All photocatalytic reactions were performed as follows: 500 mg L⁻¹ catalyst, 50 mg L⁻¹ Cr(VI) solution, 400 mg L⁻¹ phenol (for control experiments), pH = 2, 20 °C, UV-vis or visible light irradiation. (For interpretation of the references to colour in this figure legend, the reader is referred to the web version of this article.)

molecules ($E^\circ (\cdot\text{OH}/\text{H}_2\text{O}) = 1.92$ V) [49] by the photogenerated holes. Given the Cr(VI) reduction ($4.0 \mu\text{mol h}^{-1}$) and O_2 evolution ($2.6 \mu\text{mol h}^{-1}$) rate efficiency of the ZFO MNAs catalyst and the reaction proceeds through Eq. (4), we found that during UV-vis illumination an $\sim 85\%$ of surface-reaching holes are participated in water oxidation reaction to produce O_2 , while the remainder react with $\text{OH}/\text{H}_2\text{O}_{\text{abs}}$ to produce $\cdot\text{OH}$ radicals.

To explain the observed variation in the Cr(VI) photoconversion activity presented in Fig. 3, the position of the conduction band and valence band edges of each catalyst was estimated based on electrochemical impedance spectroscopy (EIS) and optical absorption measurements. Fig. 6a displays the Mott-Schottky plots obtained at a frequency of 1 kHz and the corresponding fits of the linear regime of the inverse square capacitance ($1/C_{sc}^2$) versus applied potential (E) curves for the mesoporous spinel ferrite assemblies. Using extrapolation to $1/C_{sc}^2 = 0$, the flat-band potential (E_{FB}) of ZFO, NFO, CdFO, CoFO and MFO catalysts was calculated to be -0.17 V, 0.05 V, 0.14 V, 0.08 V and -0.31 V versus NHE (pH = 7), respectively. The electron donor density (N_d) of these catalysts deduced from the slope of the $1/C_{sc}^2$ - E curves range between 3.61×10^{16} and 1.12×10^{17} cm⁻³ (see Table S2). Noted that the positive slope of the Mott-Schottky plots indicates that all catalysts have n-type properties. In Fig. 6b, the energy band diagram for each catalyst is illustrated. Considering a heavily n-doped semiconductor (such as the spinel ferrite materials), it seems reasonable to assume that the E_{FB} potential is located very close to the CB edge (typically, E_{FB} is 0–0.1 eV lower than the bottom of the CB) [50,51]. The VB maximum was thus determined by subtracting the energy band gap

(E_g) from the E_{FB} value of the semiconductors. We used diffuse reflectance UV-vis absorption spectroscopy to investigate the optical absorption properties of the MeFO MNAs. The energy band gap values were determined by Tauc's plots [$(Fhv)^2$ versus photon energy, where F , h , and v are the Kubelka-Munk function of the reflectance, Plank constant, and light frequency, respectively] and was found to be 2.17, 1.93, 1.87, 1.34 and 1.45 eV for ZFO, NFO, CdFO, CoFO and MFO MNAs, respectively (Fig. 6a, inset).

The energy diagrams show that the CB of all the spinel ferrite MNAs is positioned well above the reduction level of Cr(VI), thus collaborating the feasibility of these materials for multi-electron reduction of Cr (VI) to Cr(III). Of particular note, the photoactivity of spinel ferrite mesoporous, except for MFO, seems to correlate with the E_{FB} onset potential and obeys the order: ZFO > NFO > CdFO ~ CoFO. Meanwhile, Fig. 6b shows that all the catalysts meet the electrochemical requirement for splitting water to oxygen, that is, the position of VB in these materials is lower than the oxidation potential of water (0.82 V vs. NHE, pH = 7). Nonetheless, the photocatalytic activity for Cr(VI) reduction from MFO MNAs is considerably low that one would expect from reduction ability of the CB electrons. In particular, MFO MNAs has the most negative flat-band potential (-0.31 V) of all examined catalysts, which reflects a higher reducing property. We attribute this difference in activity to the lower water-oxidation efficiency of the MFO catalyst. Although, the high lying E_{FB} level makes MFO a good electron donor for Cr(VI) reduction, its VB edge states very close to the thermodynamic O_2 evolution potential, and therefore, it is possible a significant portion of surface-reaching holes to be lost by



Scheme 1. Schematic representation of the Cr(VI) photoreduction mechanism over mesoporous network prepared from ZFO NPs with a diameter of 6–7 nm (ZFO MNAs).

recombination, instead of engaging in oxygen evolution reaction. Also, the VB maximum of this material, like in the case of CoFO, is more negative than the electrode potential of ·OH/H₂O_{abs} and ·OH/OH⁻ pairs, which means that MFO (and similarly the CoFO) cannot oxidize water or surface hydroxyl groups to discharge ·OH (see Fig. 6b). Overall, such kinetic and thermodynamic constraints can deteriorate the photoactivity of the catalyst.

To elucidate this possibility, we examined the Cr(VI) photoreduction activity of zinc ferrite and manganese ferrite mesoporous catalysts in the presence of phenol as a sacrificial electron donor. Since phenol exhibits a lower oxidation potential than water (precisely, the redox potential of phenol and water oxidation is 0.96 V and 0.82 V vs. NHE at pH = 7, respectively), it would be reasonable to expect that phenol oxidation reaction may facilitate an efficient utilization of surface-reaching holes. This means that oxidation of phenol can overcome the kinetic limitation of the oxygen evolution reaction [i.e., 2H₂O(l) → O₂(g) + 4H⁺(aq) + 4e⁻], and therefore, in this case, the contribution from the direct electrochemical oxidation of water by the VB holes of the catalyst could be considered negligible. Fig. 6c shows the comparison of the Cr(VI) reduction time courses for ZFO and MFO MNAs photocatalysts with 10 equiv. of phenol (with respect to HCrO₄⁻ concentration). It can be observed that, in the presence of phenol, MFO behave as a more active catalyst than ZFO for Cr(VI) reduction (the rate constant (*k*) derived from the data in Fig. 6c is $5.3 \times 10^{-3} \text{ min}^{-1}$ for MFO and $3.6 \times 10^{-3} \text{ min}^{-1}$ for ZFO, see inset of Fig. 6c), which is in accord with the increasing E_{FB} potential of the semiconductors. Additionally, results of these experiments also indicated that the performance of both ZFO and MFO MNAs catalysts was further improved with addition of phenol; under UV-vis light irradiation, a quantitatively (> 99%) conversion of Cr(VI) was achieved within 3 h. The rate enhancement in the photoreduction of Cr(VI) can be explained by the fast hole-transfer kinetics for phenol oxidation, suggesting that the photo-generated electrons govern this photocatalytic process. The Cr(VI)-bearing wastewaters often contain organic dyes, pesticides, and phenolic compounds and therefore their simultaneous redox degradation is an interesting task. The ZFO and MFO MNAs materials are proven to perform as efficient photocatalysts with reasonable Cr(VI) reduction activity in these conditions. Because of the visible light response of zinc ferrite and manganese ferrite NPs (E_g ~ 2.17 eV and ~1.45 eV, respectively, as estimated by optical absorption spectra), ZFO and MFO MNAs catalysts can also perform Cr(VI) photoreduction with reasonable activity under visible light illumination. As shown in Fig. 6c, under $\lambda > 420 \text{ nm}$ light, a ~70% and a ~76% Cr(VI) conversion level was obtained with ZFO ($k = 2.3 \times 10^{-3} \text{ min}^{-1}$) and MFO ($k = 3.5 \times 10^{-3} \text{ min}^{-1}$) MNAs catalyst in 4 h, respectively.

Moreover, the ZFO MNAs catalyst is operationally stable over the course of the photoreduction. The stability of the ZFO MNAs was

assessed within three recycling experiments in the absence and presence of 0.4 g L⁻¹ phenol (Fig. 6d). The catalyst was isolated by centrifugation or using an external magnet after completion of the reaction (inset photos in Fig. 6d), washed with water, and then reused for the next catalytic run. All these photocatalytic reactions conducted under similar conditions, i.e., using 0.5 g L⁻¹ ZFO MNAs catalyst and 50 mg L⁻¹ Cr(VI) solution, manifested almost the same photoconversion yield. Evidently, the ZFO MNAs catalyst showed an improved stability with no signs of decreasing the catalytic activity after 12 h of irradiation; the rate constants of the repeated reactions were determined to be 2.3×10^{-3} (3.6×10^{-3} with phenol), 2.4×10^{-3} (4.1×10^{-3}) and 2.3×10^{-3} (4.7×10^{-3}) min⁻¹ for the 1st, 2nd and 3rd run, respectively, see upper inset of Fig. 6d. Further, XRD and N₂ porosimetry characterizations of the reused sample indicated that its crystallinity and porous structure are widely retained after catalysis, see Figs. S8 and S9. Also, EDS analysis on the retrieved catalyst (collected using a magnet without washing) indicated the nominal composition of the sample (ZnFe₂O₄), with almost no sign of Cr deposition (Fig. S10). This result, along with the control experiment (without irradiation) in Fig. S6a, suggests that adsorption of Cr(VI) ions on the catalyst's surface plays a negligible role in the photocatalytic reaction.

Based on the above results, we propose a reaction mechanism for the photocatalytic Cr(VI) reduction over spinel ferrite catalysts. Scheme 1 illustrates the mechanistic model behind the ZFO MNAs-catalyzed Cr (VI) photoreduction. Briefly, upon UV and visible light irradiation, photoexcited electrons and holes are generated in the CB and VB, respectively, of the spinel ferrite NPs. Because of the favorable electrochemical potential of the CB edge, the photoexcited electrons can be readily transferred to the catalyst surface, where they will react with harmful Cr(VI) species; as shown in Fig. 6b, the CB edge of all catalysts is more negative than the HCrO₄⁻/Cr³⁺ redox couple. On the other hand, since the VB level of the catalyst is more positive than the O₂/H₂O redox potential, the photogenerated holes react with surface adsorbed water to produce oxygen. This can be explicitly supported by results in Fig. 5a and b, which show that UV-vis light illumination of the ZFO MNAs leads to an explicit evolution of oxygen gas. Also, during the reaction, a fraction of surface-trapped holes also reacts directly with ·OH/H₂O_{abs} to produce ·OH radicals. The production of ·OH radicals in the Cr(VI)/ZFO MNAs catalytic system has been elucidated earlier by intercepting photochemically produced umbelliferone with fluorescence spectroscopy (Fig. 5d). It should be noted that, although ·OH radicals can form H₂O₂, i.e. by the reaction ·OH(aq) + ·OH(aq) → H₂O₂(aq), the production of H₂O₂ is not expected or would be minimal in this system due to the strong peroxidase-like activity of ZFO [52]. Meanwhile, the *in situ* generated ·OH radicals can also be considered as a strong oxidant for the photodegradation of organic pollutants, such as phenol. Since phenol is a better hole scavenger as compared to water, the addition of such molecules to the reaction mixture can remarkably enhance the intrinsic hole transfer efficiency, thus accelerating the overall photocatalytic process.

4. Conclusions

In summary, we succeeded in preparing high-surface-area mesoporous networks of spinel ferrite NPs from a block copolymer-directed aggregating self-assembly of colloidal nanocrystals. These nanoarchitectures are solely constructed of a continuous mesoporous network consisting of connected NPs (ca. 6–8 nm in average diameter), which provides a spatial delocalization of charge-carriers and a high surface area ($105\text{--}159 \text{ m}^2 \text{ g}^{-1}$) accessible to the reactants. We for the first time show that mesoporous assemblies made of zinc ferrite (ZnFe₂O₄) NPs perform as a viable photocatalyst, attaining improved Cr(VI) reduction photocatalysis and excellent cyclic stability without the additional use of additives (hole scavenges). Indeed, the unprecedented activity of ZFO MNAs towards Cr(VI) photoreduction is attributed to its suitable band edge positions, 3D interconnected porous structure, large internal

surface area (up to $159\text{ m}^2\text{ g}^{-1}$), and small grain composition (ca. 6–8 nm in size). Control catalytic experiments coupled with transient gas analysis and fluorescence spectroscopy data showed that Cr(VI) photoreduction reaction proceeds simultaneously with the competitive formation of O_2 and $\cdot\text{OH}$ radicals via a hole-mediated oxidation of adsorbed water or hydroxyl groups on the catalyst surface. Moreover, an addition of phenol favors the oxidation half-reaction through an efficient utilization of surface-reaching holes, which is beneficial to the acceleration of the photocatalytic reaction. The results demonstrate spinel ferrite NP assemblies as a highly efficient and stable photocatalytic system for solar light-driven environmental pollution purification and energy conversion.

Acknowledgements

This work was financially supported by the Greek Ministry of Education and the European Union under the ERC grant schemes (ERC-09), University of Crete – Special Account for Research (KA 4121) and Nanyang Technological University under the “Tan Chin Tuan Exchange Fellowship” (FY2016).

Appendix A. Supplementary data

Supplementary data associated with this article can be found, in the online version, at <https://doi.org/10.1016/j.apcatb.2018.01.045>.

References

- [1] J.J. Testa, M.A. Grela, M.I. Litter, Environ. Sci. Technol. 38 (2004) 1589–1594.
- [2] S.A. Katz, H.J. Salem, Appl. Toxicol. 13 (1993) 217–224.
- [3] J. Shang, W. Hao, X. Lv, T. Wang, X. Wang, Y. Du, S. Dou, T. Xie, D. Wang, J. Wang, ACS Catal. 4 (2014) 954–961.
- [4] J.R. Memon, S.Q. Memon, M.I. Bhanger, M.Y. Khuhawar, P. Banana, Anal. Environ. Chem. 9 (2008) 20–25.
- [5] M.S. Siboni, S. Azizian, S.M. Lee, Environ. Eng. Res. 16 (2011) 55–60.
- [6] K. Kabra, R. Chaudhary, R.L. Sawhney, Ind. Eng. Chem. Res. 43 (2004) 7683–7696.
- [7] B. Sun, E.P. Reddy, P.G. Smirniotis, Environ. Sci. Technol. 39 (2005) 6251–6259.
- [8] S. Wang, Z. Wang, W. Zhuang, Appl. Catal. B: Environ. 1 (1992) 257–270.
- [9] K. Kabra, R. Chaudhary, R. Sawhney, Ind. Eng. Chem. Res. 43 (2004) 7683–7696.
- [10] Y.C. Zhang, J. Li, M. Zhang, D.D. Dionysiou, Environ. Sci. Technol. 45 (2011) 9324–9331.
- [11] C.G. Silva, R. Juarez, T. Marino, R. Molinari, H. Garcia, J. Am. Chem. Soc. 133 (2011) 595–602.
- [12] I. Kornarakis, I.N. Lykakis, N. Vordos, G.S. Armatas, Nanoscale 6 (2014) 8694–8703.
- [13] G. Chen, M. Sun, Q. Wei, Z. Ma, B. Du, Appl. Catal. B: Environ. 125 (2012) 282–287.
- [14] M.I. Litter, Appl. Catal. B: Environ. 23 (1999) 89–114.
- [15] C. Pereira, A.M. Pereira, C. Fernandes, M. Rocha, R. Mendes, M.P. Fernández-García, A. Guedes, P.B. Tavares, J.-M. Grenèche, J.P. Araiço, C. Freire, Chem. Mater. 24 (2012) 1496–1504.
- [16] H. Zhu, S. Zhang, Y.-X. Huang, L. Wu, S. Sun, Nano Lett. 13 (2013) 2947–2951.
- [17] B. Wang, Q. Song, B. Luo, X. Li, M. Liang, X. Feng, M. Wagner, K. Müllen, L. Zhi, Chem. Asian J. 8 (2013) 410–413.
- [18] B. Jiang, C. Han, B. Li, Y. He, Z. Lin, ACS Nano 10 (2016) 2728–2735.
- [19] M.M. Vadiyar, S.S. Kolekar, J.-Y. Chang, Z. Ye, A.V. Ghule, ACS Appl. Mater. Interfaces 9 (2017) 26016–26028.
- [20] M.M. Vadiyar, S.C. Bhise, S.S. Kolekar, J.-Y. Chang, K.S. Ghule, A.V. Ghule, J. Mater. Chem. A 4 (2016) 3504–3512.
- [21] D.H.K. Reddy, Y.-S. Yun, Coord. Chem. Rev. 315 (2016) 90–111.
- [22] A.M. Kulkarni, U.V. Desai, K.S. Pandit, M.A. Kulkarni, P.P. Wadgaonkar, RSC Adv. 4 (2014) 36702–36707.
- [23] X. Guo, H. Zhu, Q. Li, Appl. Catal. B: Environ. 160–161 (2014) 408–414.
- [24] Y. Hou, X. Li, Q. Zhao, G. Chen, Appl. Catal. B: Environ. 142–143 (2013) 80–88.
- [25] C. Cai, Z. Zhang, J. Liu, N. Shan, H. Zhang, D.D. Dionysiou, Appl. Catal. B: Environ. 182 (2016) 456–468.
- [26] L. Kong, Z. Jiang, T. Xiao, L. Lu, M.O. Jonesac, P.P. Edwards, Chem. Commun. 47 (2011) 5512–5514.
- [27] K.-T. Lee, X.-F. Chuah, Y.-C. Cheng, S.-Y. Lu, J. Mater. Chem. A 3 (2015) 18578–18585.
- [28] T.-H. Yu, W.-Y. Cheng, K.-J. Chao, S.-Y. Lu, Nanoscale 5 (2013) 7356–7360.
- [29] J. Hun Kim, J.H. Kim, J.-W. Jang, J.Y. Kim, S.H. Choi, G. Magesh, J. Lee, J.S. Lee, Adv. Energy Mater. 5 (2015) 1401933.
- [30] Y. Hou, X.-Y. Li, Q.-D. Zhao, X. Quan, G.-H. Chen, Adv. Funct. Mater. 20 (2010) 2165–2174.
- [31] K.J. McDonald, K. Choi, Chem. Mater. 23 (2011) 4863–4869.
- [32] D. Yang, J. Feng, L. Jiang, X. Wu, L. Sheng, Y. Jiang, T. Wei, Z. Fan, Adv. Funct. Mater. 25 (2015) 7080–7087.
- [33] I.T. Papadas, I. Vamvasakis, I. Tamiolakis, G.S. Armatas, Chem. Mater. 28 (2016) 2886–2896.
- [34] I. Tamiolakis, I.T. Papadas, K. Spyridopoulos, G.S. Armatas, RSC Adv. 6 (2016) 54848–54855.
- [35] I.T. Papadas, S. Fountoulaki, I.N. Lykakis, Chem. Eur. 2 (2016) 4600–4607.
- [36] I. Vamvasakis, B. Liu, G.S. Armatas, Adv. Funct. Mater. 26 (2016) 8062–8071.
- [37] C. Liu, B. Zou, A.J. Rondinone, Z.J. Zhang, J. Phys. Chem. B 104 (2000) 1141–1145.
- [38] I.T. Papadas, K.S. Subrahmanyam, M.G. Kanatzidis, G.S. Armatas, Nanoscale 7 (2015) 5737–5743.
- [39] S. Brunauer, L.S. Deming, W.E. Deming, E. Teller, J. Am. Chem. Soc. 62 (1940) 1723–1732.
- [40] P.I. Ravikovich, D. Wei, W.T. Chueh, G.L. Haller, A.V. Neimark, J. Phys. Chem. B 101 (1997) 3671–3679.
- [41] P. Kubelka, J. Opt. Soc. Am. 38 (1948) 448–457.
- [42] O. Glatter, O. Kratky, Small Angle X-Ray Scattering, Academic Press, London, 1982.
- [43] K. Sun, I.A. Moreno-Hernandez, W.C. Schmidt Jr., X. Zhou, J.C. Crompton, R. Liu, F.H. Saadi, Y. Chen, K.M. Papadantonakis, N.S. Lewis, Energy Environ. Sci. 10 (2017) 987–1002.
- [44] M. Milanovic, I. Stijepovic, V. Pavlovic, V.V. Srdic, Proc. Appl. Ceram. 10 (2016) 278–293.
- [45] A.K. Srivastava, M. Deepa, N. Bahadur, M.S. Goyat, Mater. Chem. Phys. 114 (2009) 194.
- [46] P.M. Wood, Biochem. J. 253 (1988) 287–289.
- [47] G. Velegakis, J. Miao, Ch. Drivas, B. Liu, S. Kennou, G.S. Armatas, Appl. Catal. B: Environ. 221 (2018) 635–644.
- [48] S. Kim, W. Choi, Environ. Sci. Technol. 36 (2002) 2019–2025.
- [49] A. Fujishim, X.T. Zhang, C. R. Chim. 9 (2006) 750–760.
- [50] A.W. Luo, Z. Li, X. Jiang, T. Yu, L. Liu, X. Chen, J. Ye, Z. Zou, Phys. Chem. Chem. Phys. 10 (2008) 6717–6723.
- [51] A. Ishikawa, T. Takata, J.N. Kondo, M. Kara, H. Kobayashi, K. Domen, J. Am. Chem. Soc. 124 (2002) 13547–13553.
- [52] L. Su, J. Feng, X. Zhou, C. Ren, H. Li, X. Chen, Anal. Chem. 84 (2012) 5753–5758.